RSC Advances

PAPER

View Article Online
View Journal | View Issue

Cite this: *RSC Adv.*, 2017, **7**, 145

Enhanced *p*-cresol photodegradation over BiOBr/Bi_2O_3 in the presence of rhodamine B†

Aijuan Han,[ab] Jiulong Sun,[ab] Gaik Khuan Chuah*[a] and Stephan Jaenicke*[a]

Received 7th October 2016
Accepted 3rd November 2016

DOI: 10.1039/c6ra24852g

www.rsc.org/advances

Bismuth oxide is a visible-light activated photocatalyst that is adversely affected by a high rate of electron–hole recombination. To mitigate this, BiOBr/Bi_2O_3 composites were synthesized where BiOBr formed submicron thick platelets at the surface of the Bi_2O_3 particles. XRD measurements show the preferential formation of a (110)-facetted BiOBr overlayer which can be attributed to the commensurate structure of this plane with the (120) plane of Bi_2O_3. The photodegradation of *p*-cresol and RhB was studied as representative of an organic pollutant and a dye, respectively. The composite with 85% BiOBr/Bi_2O_3 exhibited the highest photoactivity for both molecules. Its higher activity compared to that of either Bi_2O_3 or BiOBr alone, or a mechanical mixture with the same composition, supports the hypothesis that the formation of an hetero-epitactic interface between BiOBr and Bi_2O_3 is instrumental in reducing electron–hole pair recombination. Interestingly, in mixtures of *p*-cresol and RhB, the rate of *p*-cresol photodegradation was enhanced but that for RhB was decreased compared to the pure solutions. This is not caused by competitive adsorption of the molecules but rather by excitation transfer from RhB to the co-adsorbed *p*-cresol. Therefore, the RhB degradation by deethylation, which is a surface reaction, is suppressed and only the reaction channel through attack of the OH· radical at the aromatic chromophore remains open.

1. Introduction

Water pollution is a pressing issue worldwide. Developing cheap and efficient ways to degrade pollutants has become the center point of much research.[1] Semiconductor photocatalysis can be conveniently applied for the degradation of organic pollutants in water. Among various semiconductors, TiO_2 has been most extensively used due to its photoactivity, insolubility, stability, low cost and non-toxic nature.[2,3] Unfortunately, TiO_2 has a wide band gap of 3.0–3.2 eV and is therefore not well matched to the solar spectrum. Only a small fraction (*ca.* 4%) of the incoming solar energy lies in the ultraviolet region, whereas visible light (400–700 nm) is far more abundant (*ca.* 46%). Hence, the research focus has shifted to the development of photocatalysts that can be activated by visible light.

Several bismuth compounds have been reported to be visible light active photocatalysts, such as bismuth oxyhalides,[4–8] $NaBiO_3$,[9–12] $BiVO_4$,[13–16] *etc.* It is interesting that despite being a heavy metal, bismuth is generally considered to be safe, as it is non-toxic and noncarcinogenic.[17] In fact, bismuth salts are widely used in pharmaceutical products as antacids and in the treatment of peptic ulcers. Besides the ternary compounds, mixtures and composites such as $NaBiO_3$/BiOCl,[18] BiOI/BiOCl,[19,20] BiOCl/BiOBr[21–25] and Bi/BiOBr[26] have been investigated for their photoactivity.

Bismuth oxide (Bi_2O_3) has a narrow band gap of ~2.8 eV and has been used as a visible-light active photocatalyst for the degradation of organic pollutants, water splitting and organocatalysis.[27–31] However, its photoactivity is hampered by fast electron–hole pair recombination. To facilitate the separation of the photo-generated electrons and holes, Bi_2O_3 has been coupled with other semiconductors in systems such as BiOCl/Bi_2O_3,[32] BiOI/Bi_2O_3,[33] Bi_2O_3/Co_3O_4,[34] Bi_2O_3-reduced graphene oxide,[35] Bi_2O_3/TiO_2,[36,37] or Bi_2O_3/Bi_2O_{4-x}.[38] These examples motivated us to examine Bi_2O_3 more closely as a photocatalyst. We chose to investigate composite systems of BiOBr and Bi_2O_3, both of which absorb visible light as their band gaps are in the range of 2.8–2.9 eV. Wang *et al.* recently reported a similar system but their BiOBr/Bi_2O_3 composites were only 2.06 and 1.83 times more active for photodegradation of methyl orange than Bi_2O_3 and BiOBr, respectively.[39] To achieve a high degree of cohesion at the interfaces within the composite, solid Bi_2O_3 was chemically converted to BiOBr by etching with varying amounts of HBr. Electronic structures were calculated using Density Functional Theory as implemented in the CASTEP code of the Materials Studio software (Fig. S1†). Bi_2O_3 has a direct band gap while BiOBr has an indirect band gap. The valence band of

[a]*Department of Chemistry, National University of Singapore, 3 Science Drive 3, Singapore 117543, Singapore. E-mail: chmcgk@nus.edu.sg; chmsj@nus.edu.sg; Fax: +65 6779 1691; Tel: +65 6516 2839; +65 6516 2918*

[b]*NUS Environmental Research Institute, National University of Singapore, 5A Engineering Drive 1, #02-01, Singapore 117411, Singapore*

† Electronic supplementary information (ESI) available. See DOI: 10.1039/c6ra24852g

Bi_2O_3 is mainly due to oxygen 2p orbitals, whereas the valence band of BiOBr is mainly generated from bromine 4p (Fig. S2†). Hence, the valence band level of Bi_2O_3 is expected to be more negative than that of BiOBr. This is supported by the band edge positions of Bi_2O_3 and BiOBr as predicted using the Mulliken electronegativity of the individual atoms:[40]

$$E_{VB} = \chi - E^e + (1/2)E_g$$

where χ, the electronegativity of the semiconductor, is calculated from the geometric mean of the electronegativities of the elements in the semiconductor, E^e is the energy of free electrons on the hydrogen scale ($\approx$4.5 eV), and E_g is the band gap energy of the semiconductor. The calculated conduction band and valence band edge positions for Bi_2O_3 and BiOBr are shown in Fig. 1. As the conduction band of Bi_2O_3 is more negative (−0.04 eV) than that of BiOBr (0.26 eV), electrons from Bi_2O_3 can transfer to BiOBr. In addition, holes formed in the valence band of BiOBr can move to the more negative valence band of Bi_2O_3. The relative positions of the conduction and valence bands indicate that photoinduced electron–hole pairs can be effectively separated at the interface of the two semiconductors. This should reduce direct electron–hole recombination and, consequently, increase the quantum efficiency. Furthermore, because of its more positive valence band, composites with BiOBr as the main component are expected to have stronger oxidation potential that can be used for the degradation of organic pollutants.

Dyes are important water pollutants because they are resistant to biodegradation and direct photolysis. Natural reductive anaerobic degradation of many N-containing dyes such as rhodamine B is (RhB) incomplete and often generates potentially carcinogenic aromatic amines. However, the use of dyes to assess visible-light activated photocatalysts may not be appropriate due to dye sensitization. Hence, we used *p*-cresol as a model pollutant to assess the photoactivity of BiOBr/Bi_2O_3 with different compositions. Cresols are found in disinfectants, herbicides, wood preservatives and formulations for fragrances and dyes.[41] For the purpose of benchmarking with other photocatalysts reported in the literature, the best photocatalyst was also tested using RhB.

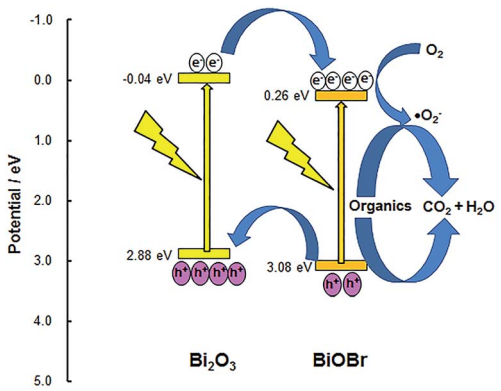

Fig. 1 Band gap and possible charge flow within the BiOBr/Bi_2O_3 heterojunction.

2. Experimental

2.1 Sample preparation

The BiOBr/Bi_2O_3 heterojunctioned composites were prepared by reacting Bi_2O_3 with hydrobromic acid. After dispersing 1.398 g (3 mmol) of crystalline bismuth oxide (Sigma-Aldrich) in 14 ml of absolute ethanol, the required volume of 33% hydrobromic acid in glacial acetic acid (containing 1.5 to 6 mmol HBr) was added dropwise with stirring. The suspension was stirred for 1 h and the solid was recovered by centrifugation, washed with absolute ethanol and dried at 80 °C overnight in an oven. Pure BiOBr was prepared by etching Bi_2O_3 for 4 days in an excess (18 mmol) of hydrobromic acid/acetic acid solution.

2.2 Characterization

Powder X-ray diffraction patterns were measured with a Siemens D5005 diffractometer using Cu K_α radiation for 2θ between 10 to 70° at 0.02° per step and a dwell time of 1 s per step. A calibration plot using the peak areas of the most intense reflexes, *i.e.*, $2\theta \sim 27.5°$ for Bi_2O_3 and 31.7° for BiOBr, was made from known amounts of pure Bi_2O_3 and BiOBr. Based on this, the percentage of Bi_2O_3 and BiOBr in the composites was determined. Nitrogen adsorption and desorption isotherms were measured at −196 °C using a TriStar 3000 (Micromeritics) porosimeter. The specific surface area was calculated according to the BET (Brunauer–Emmett–Teller) model. Scanning electron micrographs were obtained with a JEOL JSM-6701F SEM (field-emission). Transmission electron microscopy was carried out using a JEOL 3010 transmission electron microscope operated at 200 kV. About 5 mg of finely ground sample was suspended in 5 ml of 2-propanol and after sonication, a drop of the suspension was placed onto a carbon-coated copper grid and dried at room temperature overnight. Diffuse reflectance spectra were measured with a Shimadzu UV-2450 UV-visible spectrophotometer.

2.3 Photocatalytic activity

The photoactivity was measured using a 250 ml cylindrical quartz reactor at room temperature in air. Typically, a suspension of 0.10 g photocatalyst in 100 ml of an aqueous solution containing 24 ppm of *p*-cresol was magnetically stirred for 1 h to establish an adsorption–desorption equilibrium. The reactor was then irradiated by a 22 W daylight fluorescent lamp (KES). The photon flux had been determined with the potassium ferrioxalate actinometer system assuming a Fe^{3+} quantum yield of 1.11. To follow the photodegradation, aliquots were withdrawn at specific time intervals, centrifuged and the concentration of *p*-cresol determined from its absorption band at $\lambda = 277.5$ nm using a UV-vis spectrophotometer (Shimadzu UV1601) or by high performance liquid chromatography (Shimadzu UFLC 20A) with a mobile phase of acetonitrile and water (50 : 50, v/v) at a flow rate of 1.0 ml min^{-1} and a Shim-pack VP-ODS C-18 reverse-phase column (250 mm l × 4.6 mm i.d., 5 μm). Besides *p*-cresol, RhB (20 ppm) and mixtures of RhB and *p*-cresol were similarly tested using the fluorescent, as well as

blue, green and red LED lamps. The degradation efficiency (DE) was calculated as:

$$DE = (C_0 - C)/C_0 \times 100\%$$

where C_0 is the concentration of *p*-cresol before irradiation but after the adsorption equilibrium, and C is the *p*-cresol concentration at time t. Pseudo first-order kinetics were applied to the degradation according to the equation: $\ln(C_0/C) = kt$ where k is the pseudo-first-order rate constant. The quantum yield was calculated from the number of *p*-cresol molecules degraded divided by the total incoming photons from the lamp (5.2×10^{16} photons per s). The recyclability of the catalyst was tested by adding fresh *p*-cresol after the reaction, allowing again an hour in the dark for adsorption before analyzing the solution at regular intervals during irradiation.

3. Results and discussion

3.1 Characterization

The powder X-ray diffraction patterns of pure Bi_2O_3 and BiOBr agree well with those of monoclinic α-Bi_2O_3 (PDF 65-2366) and tetragonal BiOBr (PDF 73-2061), respectively (Fig. 2). For the BiOBr/Bi_2O_3 composites, no other phases except Bi_2O_3 and BiOBr were observed. By changing the molar ratio of HBr to Bi_2O_3 from 0.5 to 2 during the synthesis, the amount of BiOBr in the composite increased from 12 to 85 wt% (Fig. S3†). Pure BiOBr was obtained with HBr/Bi_2O_3 of 6.

In the XRD diffractogram of α-Bi_2O_3, the (120) reflex at $2\theta \sim 27.5°$ has the by far highest intensity, indicating the prevalence of this plane. With 12 wt% BiOBr in the composite, the (110) peak at $2\theta \sim 32.4°$ was the only BiOBr peak that could be observed. At higher BiOBr amounts in the composites, additional BiOBr peaks can be seen. In particular, the (102) peak at $2\theta \sim 31.7°$ grew to become the strongest peak for pure BiOBr. The dominance of (110)-facetted BiOBr at low HBr concentration may be attributed to commensurate atomic packing with the underlying Bi_2O_3. The (120) plane in Bi_2O_3 is made up of single zigzagging rows of Bi separated by double rows of oxygen (Fig. 3a). For the (110) plane of BiOBr, single rows of Bi are separated by double rows of bromine with only a slight increase in the Bi–Bi distance from 8.11 Å in Bi_2O_3 to 8.13 Å in BiOBr. However, the (102) plane of BiOBr which formed at higher BiOBr content bears little similarity to the (120) plane of Bi_2O_3 (Fig. 3b).

The commercial Bi_2O_3 has a low surface area of 2.30 $m^2\ g^{-1}$ (Table 1). SEM micrographs of the material show irregular micro-sized particles (Fig. 4). After etching with HBr, the surface area of the composites increased to 3.00–7.99 $m^2\ g^{-1}$. The increase in surface area of the BiOBr/Bi_2O_3 composites can be attributed to the formation of densely packed BiOBr platelets orientated in whorls perpendicular to the surface of the original Bi_2O_3 particles (Fig. 4). The thickness of these platelets grew with higher BiOBr content (from 15–20 nm to 60–100 nm). Due to the difference in the density of Bi_2O_3 (8.90 g cm^{-3}) and BiOBr (6.70 g cm^{-3}), the newly formed BiOBr occupies a larger volume than the Bi_2O_3 particles and contributes to the increased surface area. However, the pure BiOBr that formed after extensive contact of Bi_2O_3 with HBr had a very low surface area of only 0.67 $m^2\ g^{-1}$. The sample comprised of plate-like particles with dimensions of 0.5–3 μm and 150–500 nm thickness.

TEM was used to analyze the interface between the two phases in the composites. The micrograph of an 85% BiOBr/Bi_2O_3 sample clearly shows two different lattice spacings (Fig. 5). The lattice spacing of 0.28 nm corresponds to the (110) lattice plane of tetragonal BiOBr and is prevalent throughout the particle while the 0.33 nm lattice spacing can be assigned to the (120) lattice plane of Bi_2O_3. The latter only covers parts of the particle. The selective area electron diffraction (SAED) pattern shows spots which can be assigned to single crystalline BiOBr and diffraction rings that can be indexed to crystal planes of Bi_2O_3. Hence, these results lend support that Bi_2O_3 and BiOBr are well mixed at the nanoscale level, with BiOBr being the major component.

3.2 Optical properties

The optical absorption of a semiconductor near the band gap edge is given by the formula $\alpha h\nu = A(h\nu - E_g)^{\eta}$, where $\alpha =$

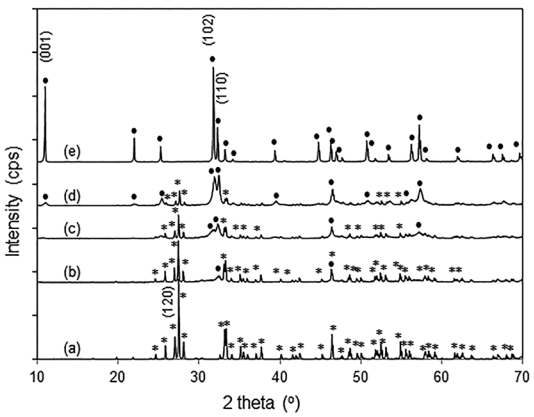

Fig. 2 XRD patterns of (a) Bi_2O_3 (*), (b) 12% BiOBr/Bi_2O_3, (c) 57% BiOBr/Bi_2O_3, (d) 85% BiOBr/Bi_2O_3, and (e) BiOBr (●).

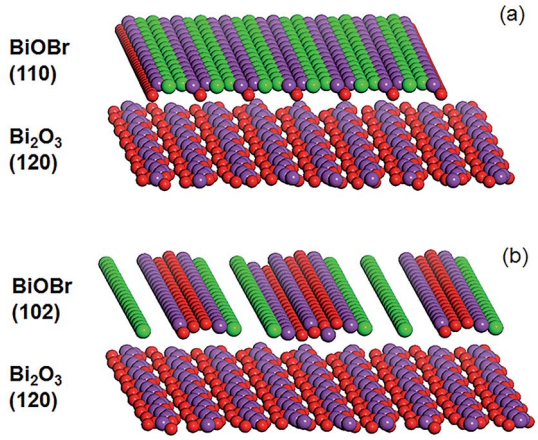

Fig. 3 Illustration of the Bi_2O_3 (120) and BiOBr (a) (110) and (b) (102) planes (color code: red: O, purple: Bi, and green: Br).

Table 1 Physical properties of the photocatalysts

Sample	Surf. area ($m^2\ g^{-1}$)	Amt. adsorbed[a] ($\mu mol\ m^{-2}$)	
		p-cresol	RhB
Bi_2O_3	2.28	5.2	1.1
12% BiOBr/Bi_2O_3	3.00	4.3	2.1
57% BiOBr/Bi_2O_3	4.81	2.7	2.0
85% BiOBr/Bi_2O_3	7.99	1.0	1.9
BiOBr	0.67	3.2	2.2
85/15 BiOBr/Bi_2O_3[b]	1.01	3.1	1.9

[a] After 1 h in dark. [b] Mechanical mixture.

absorption coefficient, ν = light frequency, E_g = band-gap energy, A = constant and $\eta = \{1/2, 3/2, 2, 3\}$, for transitions that are direct-allowed, direct-forbidden, indirect-allowed and indirect-forbidden, respectively.[42] The Kubelka–Munk function, $F(R_\infty)$, for infinitely thick samples, is related to α by $F(R_\infty) = (1 - R_\infty)^2/2R_\infty = \alpha/S$ where R_∞ is the reflectance of the sample divided by the reflectance of $BaSO_4$ which is used as a reference, and S = scattering coefficient. As the scattering coefficient depends only weakly on energy, $F(R_\infty)$ is proportional to α within the narrow energy range containing the absorption edge. By using the appropriate value for the exponent η, a plot of $(F(R_\infty)h\nu)^{1/\eta}$ *versus* $h\nu$ results in a straight line where the intercept with the *x*-axis gives the band gap energy. Bi_2O_3, BiOBr and the composites all absorb in the visible light region with the absorption edge between 380 and 470 nm (Fig. 6a). For Bi_2O_3, the best linear fit was obtained with $\eta = 1/2$, in agreement with a direct-allowed electron transition of the material, and the E_g was deduced to be 2.92 eV (Fig. 6b). Because the band gap transition in BiOBr is indirect, a linear fit was obtained with $\eta = 2$ and the E_g was calculated to be 2.82 eV. Despite the wider band gap in Bi_2O_3, its absorption in the visible light region of 400–500 nm is stronger than that of BiOBr due to the direct excitation of electrons. The absorption of BiOBr/Bi_2O_3 composites decreased with BiOBr content and these materials have two band gaps between 2.82 and 2.92 eV.

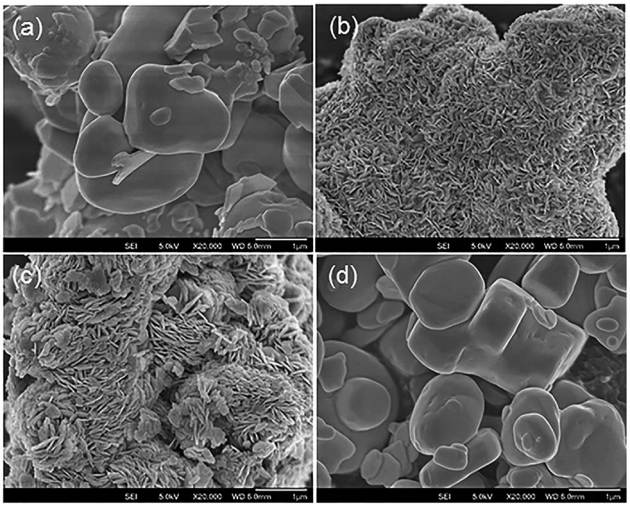

Fig. 4 SEM of (a) pure Bi_2O_3, (b) 12% BiOBr/Bi_2O_3, (c) 85% BiOBr/Bi_2O_3, and (d) BiOBr.

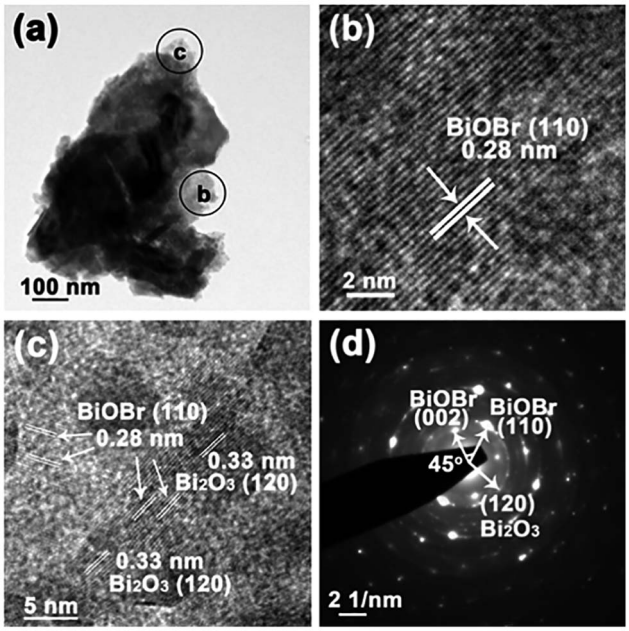

Fig. 5 (a) TEM (b and c) HRTEM and (d) SAED of 85% BiOBr/Bi_2O_3.

3.3 Photocatalytic properties

In the absence of the photocatalyst, no *p*-cresol degradation occurred even after 14 h illumination with visible light. In the presence of Bi_2O_3, ~49% of *p*-cresol was degraded after this time (Fig. 7a). The degradation efficiency of the BiOBr/Bi_2O_3 composites was significantly higher and increased with BiOBr composition. However, pure BiOBr gave only 34% degradation efficiency. The highest activity was observed for 85 wt% BiOBr/Bi_2O_3 where 33% of *p*-cresol was degraded within 2 h and 94% after 14 h.

The photodegradation of RhB was considerably faster than that of *p*-cresol. The highest photoactivity for RhB degradation was again observed for the sample, 85 wt% BiOBr/Bi_2O_3,

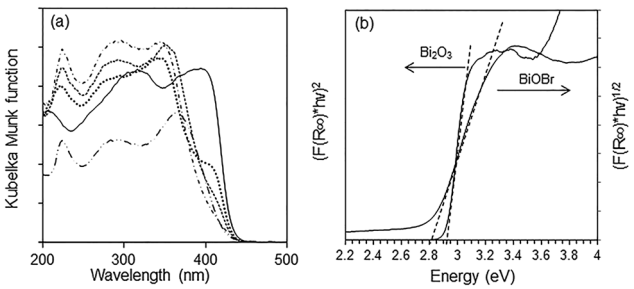

Fig. 6 (a) Diffuse reflectance spectra of (—) Bi_2O_3, (– · · –) BiOBr, BiOBr/Bi_2O_3 composites with (••) 12%, (- - -) 57% and (- • -) 85% BiOBr and (b) determination of absorption edge energies for Bi_2O_3 and BiOBr.

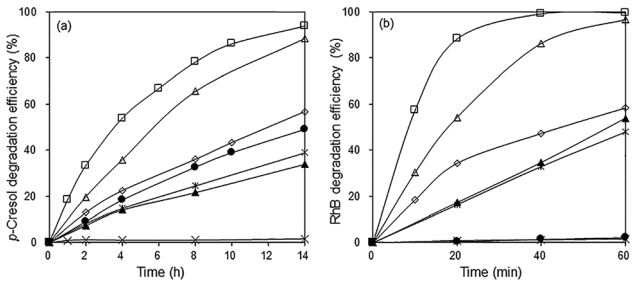

Fig. 7 Photocatalytic degradation of (a) 24 ppm *p*-cresol and (b) 20 ppm RhB under visible light irradiation. (×) No catalyst, (●) Bi_2O_3, (▲) BiOBr, (◇) 12% BiOBr/Bi_2O_3, (△) 57% BiOBr/Bi_2O_3, (□) 85% BiOBr/Bi_2O_3, and (*) mechanical mixture of 85 wt% BiOBr/Bi_2O_3.

showing that its activity is not specific for only one type of molecule (Fig. 7b). After only 1 h, >99% of RhB had been degraded. BiOBr/Bi_2O_3 were mechanically mixed in the same weight ratio, but its pseudo first-order rate constants for the degradation of *p*-cresol and RhB was about 5 and 8 times smaller, respectively, than the heterojunctioned composite. This result points to the importance of heterojunctions in the composite rather than the composition. The intimately bound interface formed between the (110) planes of BiOBr with the underlying (120) planes in Bi_2O_3 can reduce the electron–hole pair recombination more effectively than the loosely formed junctions between the components in the mechanical mixture.

Interestingly, when a mixture containing 20 ppm RhB and 24 ppm of *p*-cresol was used as substrate, the rate of *p*-cresol photodegradation increased while that of RhB decreased (Fig. 8). 94% of *p*-cresol was degraded after only 6 h instead of 14 h. In contrast, RhB required 8 h instead of 1 h to reach >99% degradation efficiency. Similar results were observed when the *p*-cresol/RhB mixture was illuminated with blue, green and red LED light (Fig. S4†). With the blue LED light (wavelength of 430–470 nm), there should be no dye sensitization as the RhB does not absorb in this range (Fig. 9). Nevertheless, the apparent quantum yield for *p*-cresol degradation in the mixture was again substantially enhanced over that in the pure solution (2.53 *vs.* 0.31%).

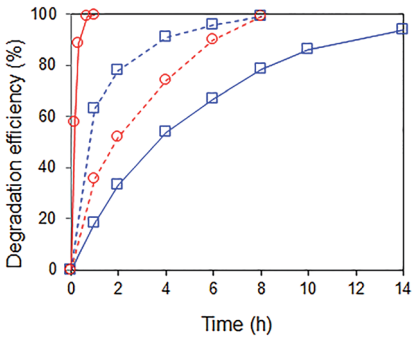

Fig. 8 Photocatalytic degradation of (□) 24 ppm *p*-cresol and (○) 20 ppm RhB under visible light irradiation (λ > 400 nm). (—) Pure solution with one substrate only and (---) mixture of 24 ppm *p*-cresol and 20 ppm RhB. Photocatalyst: 85 wt% BiOBr/Bi_2O_3.

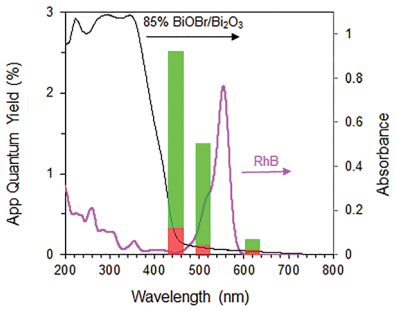

Fig. 9 Apparent quantum yield for RhB (red) and *p*-cresol (green) in mixture with 20 ppm RhB and 24 ppm *p*-cresol under blue, green and red LED light over 85% BiOBr/Bi_2O_3. Secondary *y*-axis shows absorbance of photocatalyst and RhB.

The effect of RhB on the photodegradation of *p*-cresol was further investigated using blue LED illumination. Addition of 10 and 20 ppm of RhB increased the rate of *p*-cresol photodegradation so that >95% of *p*-cresol was degraded after 10–12 h (Fig. 10a). In contrast, the photoactivity for RhB degradation was adversely affected by the simultaneous presence of *p*-cresol (Fig. 10b). Without added *p*-cresol, complete degradation of RhB occurred within 2 h but in the presence of 24 ppm *p*-cresol, it required 10 h. With 48 ppm *p*-cresol, even after 10 h, only 62% of RhB was photodegraded.

To understand the interactive effect of *p*-cresol and RhB, we examined the equilibrium surface concentrations after adsorption in the dark. Individually, the amount of adsorbed *p*-cresol and RhB on 85 wt% BiOBr/Bi_2O_3 was calculated to be 1.0 and 1.9 μmol m^{-2}, respectively (Table 1). Hence, despite a 5× lower molar concentration (42 μM RhB *vs.* 222 μM *p*-cresol), the equilibrium surface concentration for RhB is higher than for *p*-cresol. This can be explained by the electrostatic attraction between the negatively charged BiOBr/Bi_2O_3 surface, which has a point of zero charge at pH 6.1 (Fig. S5†), and the positively charged amino groups of RhB. At a solution pH of 5, RhB exists in the deprotonated form and cannot adsorb *via* the carboxylic acid group. In the mixed *p*-cresol–RhB solutions, the decreased rate of RhB photodegradation in the mixture cannot be explained by competitive adsorption between the two molecules as the adsorbed *p*-cresol and RhB at the surface fell by only ~2

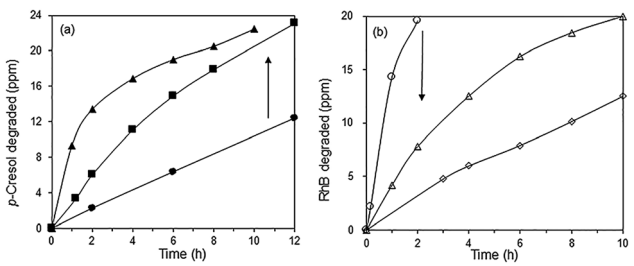

Fig. 10 Photocatalytic degradation of (a) 24 ppm *p*-cresol with (●) 0 (■) 10 (▲) 20 ppm RhB and (b) 20 ppm RhB with (○) 0 (△) 24 and (◇) 48 ppm *p*-cresol under blue LED irradiation. Photocatalyst: 85% BiOBr/Bi_2O_3.

and 5%, respectively. Moreover, the rate of *p*-cresol photodegradation was enhanced rather than decreased.

Some insights into the underlying interaction may be deduced from the spectral changes of the RhB UV-vis spectra during photodegradation over 85% $BiOBr/Bi_2O_3$. RhB shows an intense absorption band at 554 nm which decreased by ~40% due to adsorption at the surface of the photocatalyst (Fig. 11a). Upon visible light irradiation, the absorption decreased, accompanied by a shift of the peak maximum to shorter wavelengths. This hypsochromic shift has been associated with the stepwise removal of ethyl groups from RhB (*N*,*N*,*N*′,*N*′-tetraethylated rhodamine) to form rhodamine (λ_{max} ~ 498 nm).[43] After 60 min, the peak intensity decreased without any further shift in the wavelength as the ring structure of the RhB chromophore is degraded. However, in the presence of *p*-cresol, the absorbance initially decreased without any shift in the wavelength indicating that degradation occurred at the aromatic RhB chromophore.

De-ethylation of RhB is a surface process that requires the molecule to be adsorbed on the photocatalyst. Photodegradation is initiated by injection of an electron from an excited RhB into the conduction band of the photocatalyst or the adsorbed RhB molecule traps a photogenerated hole and is converted to RhB^{+}.[43] In contrast, the aromatic ring structure is cleaved by photogenerated ·OH, ·OOH and $\cdot O_2^-$ in the solution phase away from the surface.[43–45] The presence of ·OH was detected by its reaction with terephthalic acid, forming 2-hydroxyterephthalic acid which gave an intense fluorescence at 425 nm (Fig. S6†).[46] Use of scavengers showed that superoxide and especially holes also participated in the photodegradation (Fig. S7†).[47,48] However, due to their low concentrations in bulk solution, this degradative route is slower than de-ethylation. The UV-vis spectra indicate that the former occurred when *p*-cresol was added. However, electrons, holes, ·OH, and ·OOH are generated at a rate that does not depend on whether *p*-cresol or RhB is present singly or in a mixture. The changes in their degradation rates suggest RhB forms an effective conduit to transfer the surface photogenerated electrons or holes to *p*-cresol (Fig. 12). Co-adsorption at the surface of the photocatalyst is necessary to bring the molecules close enough for excitation transfer from RhB to *p*-cresol. As a result, the rate at which RhB is *N*-dealkylated is decreased while simultaneously the rate of *p*-cresol degradation is increased. Without the solid photocatalyst, no degradation was observed, showing that RhB does not act as a photosensitizer.

To confirm that in the presence of *p*-cresol, the predominant pathway for RhB degradation is *via* photogenerated oxidant species in the bulk solution, Fe^{3+} was added to a mixture of *p*-cresol and RhB. When a photoelectron reacts with oxygen, H_2O_2 is formed together with OH·:

$$e^- + O_2 \rightarrow \cdot O_2^-$$

$$\cdot O_2^- + H_2O \rightarrow HOO\cdot + OH^-$$

$$HOO\cdot + H_2O \rightarrow HO\cdot + H_2O_2$$

Although H_2O_2 is relatively unreactive, Fe^{3+} can catalyse the decomposition of H_2O_2 to generate more ·OH radicals in the bulk solution *via*:

$$Fe^{3+} + H_2O_2 \rightarrow Fe^{2+} + \cdot OOH + H^+$$

$$Fe^{3+} + \cdot OOH \rightarrow Fe^{2+} + H^+ + O_2$$

$$Fe^{2+} + H_2O_2 \rightarrow Fe^{3+} + \cdot OH + OH^-$$

A substantial acceleration of the RhB degradation was indeed observed when Fe^{3+} was added (Fig. 13) with the rate increasing with Fe^{3+} concentration. The degradation occurred *via* cleavage at the aromatic chromophore as no shift in the wavelength of RhB absorption peak at 554 nm was observed (Fig. S8†).

The stability of the photocatalyst was tested by adding fresh RhB solution after each batch reaction (Fig. S9a†). There was no significant change in the degradation efficiency over four cycles.

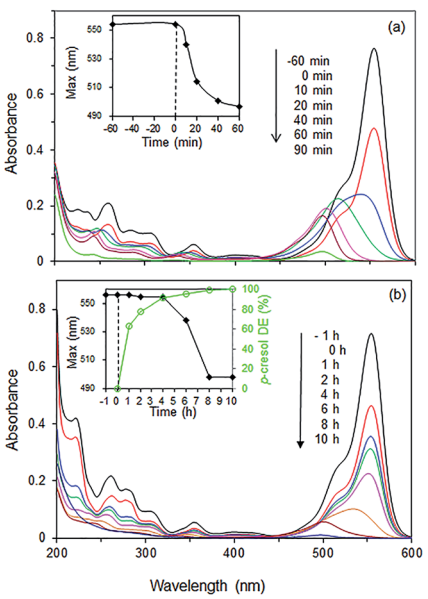

Fig. 11 UV spectra of (a) pure RhB solution and (b) mixture of RhB and *p*-cresol (20 : 24 ppm) under visible light irradiation as a function of time. Photocatalyst: 85% $BiOBr/Bi_2O_3$.

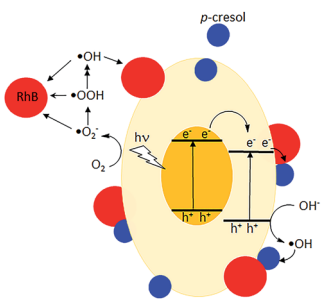

Fig. 12 Proposed degradative pathways for (●) *p*-cresol (●) and RhB.

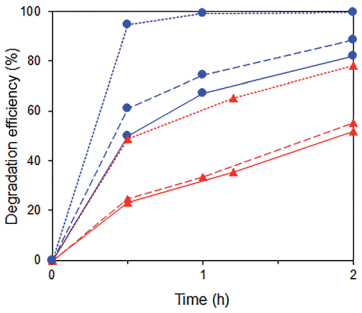

Fig. 13 Photocatalytic degradation of *p*-cresol (●) and RhB (▲) in mixtures with no Fe^{3+} (—) and in the presence of 0.016 mM (---) and 2.5 mM (··) Fe^{3+}.

The X-ray diffractogram of the used catalyst was similar to that of the fresh catalyst, indicating its stability against photocorrosion (Fig. S9b†).

4. Conclusion

The reaction of hydrobromic acid with Bi_2O_3 forms heterojunctioned composites of BiOBr and Bi_2O_3. Because of the similarity in the atomic arrangement of the (120) plane of Bi_2O_3 and the (110) plane of BiOBr, a tightly connected interface can form between the growing BiOBr overlayer and the underlying Bi_2O_3 substrate. SEM micrographs showed that the composites consisted of BiOBr platelets arranged in whorls perpendicular to the Bi_2O_3 surface. The density and thickness of these nanosized platelets increased with BiOBr content. The 85% BiOBr/Bi_2O_3 composite developed the highest photocatalytic activity for *p*-cresol and RhB. The photoactivity of the composite catalyst was much higher than that of a mechanical mixture with the same composition, supporting the concept that the interfaces are important to separate the photogenerated charge carriers. In a mixture of *p*-cresol and RhB, the photodegradation of *p*-cresol was accelerated whereas that of RhB was hindered. UV-vis studies showed that in the presence of *p*-cresol, de-ethylation of RhB was inhibited, leaving degradation of the aromatic chromophore by active species from the bulk solution.

Acknowledgements

A. Han gratefully acknowledges the support of the Singapore-Peking-Oxford Research Enterprise (SPORE) for a research assistantship. This work was supported by Ministry of Education ARC Tier 1 grants R-143-000-550-112 and R-143-000-603-112.

References

1 X. Chen and S. S. Mao, *Chem. Rev.*, 2007, **107**, 2891–2959.
2 I. Sesenoglu, O. E. Kartal, H. Oguz, M. Erol and A. Calimli, *Rev. Chem. Eng.*, 1999, **15**, 223–232.
3 A. G. Agrios and P. Pichat, *J. Appl. Electrochem.*, 2005, **35**, 655–663.
4 K. L. Zhang, C. M. Liu, F. Q. Huang, C. Zheng and W. D. Wang, *Appl. Catal., B*, 2006, **68**, 125–129.
5 J. Zhang, F. Shi, J. Lin, D. Chen, J. Gao, Z. Huang, X. Ding and C. Tang, *Chem. Mater.*, 2008, **20**, 2937–2941.
6 X. Xiao and W. Zhang, *J. Mater. Chem.*, 2010, **20**, 5866–5870.
7 X. Chang, M. A. Gondal, A. A. Al-Saadi, M. A. Ali, H. Shen, Q. Zhou, J. Zhang, M. Du, Y. Liu and G. Ji, *J. Colloid Interface Sci.*, 2012, **377**, 291–298.
8 J. Hu, S. Weng, Z. Zheng, Z. Pei, M. Huang and P. Liu, *J. Hazard. Mater.*, 2014, **264**, 293–302.
9 K. Yu, S. Yang, H. He, C. Sun, C. Gu and Y. Ju, *J. Phys. Chem. A*, 2009, **113**, 10024–10032.
10 X. Chang, J. Huang, C. Cheng, W. Sha, X. Li, G. Ji, S. Deng and G. Yu, *J. Hazard. Mater.*, 2010, **173**, 765–772.
11 X. Chang, G. Ji, Q. Sui, J. Huang and G. Yu, *J. Hazard. Mater.*, 2009, **166**, 728–733.
12 T. Kako, Z. Zou, M. Katagiri and J. Ye, *Chem. Mater.*, 2007, **19**, 198–202.
13 S. Kohtani, S. Makino, A. Kudo, K. Tokumura, Y. Ishigaki, T. Matsunaga, O. Nikaido, K. Hayakawa and R. Nakagaki, *Chem. Lett.*, 2002, **7**, 660–661.
14 J. Yu and A. Kudo, *Adv. Funct. Mater.*, 2006, **16**, 2163–2169.
15 W. Yin, W. Wang, L. Zhou, S. Sun and L. Zhang, *J. Hazard. Mater.*, 2010, **173**, 194–199.
16 X. Zhang, X. Quan, S. Chen and Y. Zhang, *J. Hazard. Mater.*, 2010, **177**, 914–917.
17 N. M. Leonard, L. C. Wieland and R. S. Mohan, *Tetrahedron*, 2002, **58**, 8373–8397.
18 X. Chang, G. Yu, J. Huang, Z. Li, S. Zhu, P. Yu, C. Cheng, S. Deng and G. Ji, *Catal. Today*, 2010, **153**, 193–199.
19 T. B. Li, G. Chen, C. Zhou, Z. Y. Shen, R. C. Jin and J. X. Sun, *Dalton Trans.*, 2011, **40**, 6751–6758.
20 X. Xiao, R. Hao, M. Liang, X. Zuo, J. Nan, L. Li and W. Zhang, *J. Hazard. Mater.*, 2012, **233**, 122–130.
21 Y. Liu, W. J. Son, J. Lu, B. Huang, Y. Dai and M. H. Whangbo, *Chem.–Eur. J.*, 2011, **17**, 9342–9349.
22 S. Shenawi-Khalil, V. Uvarov, Y. Kritsman, E. Menes, I. Popov and Y. Sasson, *Catal. Commun.*, 2011, **12**, 1136–1141.
23 H. Gnayem and Y. Sasson, *ACS Catal.*, 2013, **3**, 186–191.
24 J. Zhang, J. Xia, S. Yin, H. Li, H. Xu, M. He, L. Huang and Q. Zhang, *Colloids Surf., A*, 2013, **420**, 89–95.
25 B. Zhang, G. Ji, Y. Liu, M. A. Gondal and X. Chang, *Catal. Commun.*, 2013, **36**, 25–30.
26 X. Zhang, G. Ji, Y. Liu, X. Zhou, Y. Zhu, D. Shi, P. Zhang, X. Cao and B. Wang, *Phys. Chem. Chem. Phys.*, 2015, **17**, 8078–8086.
27 J. Eberl and H. Kisch, *Photochem. Photobiol. Sci.*, 2008, **7**, 1400–1406.
28 K. Barrera-Mota, M. Bizarro, M. Castellino, A. Tagliaferro, A. Hernandez and S. E. Rodil, *Photochem. Photobiol. Sci.*, 2015, **14**, 1110–1119.
29 L. Zhou, W. Wang, H. Xu, S. Sun and M. Shang, *Chem.–Eur. J.*, 2009, **15**, 1776–1782.
30 S. J. A. Moniz, C. S. Blackman, C. J. Carmalt and G. Hyett, *J. Mater. Chem.*, 2010, **20**, 7881–7886.
31 P. Riente, A. M. Adams, J. Albero, E. Palomares and M. A. Pericàs, *Angew. Chem., Int. Ed.*, 2014, **126**, 9767–9770.

32 S. Y. Chai, Y. J. Kim, M. H. Jung, A. K. Chakraborty, D. Jung and W. I. Lee, *J. Catal.*, 2009, **262**, 144–149.
33 Y. Li, J. Wang, H. Yao, L. Dang and Z. Li, *Catal. Commun.*, 2011, **12**, 660–664.
34 S. H. Hsieh, G. J. Lee, C. Y. Chen, J. H. Chen, S. H. Ma, T. L. Horng, K. H. Chen and J. J. Wu, *Top. Catal.*, 2013, **56**, 623–629.
35 X. Liu, L. Pan, T. Lv, Z. Sun and C. Q. Sun, *J. Colloid Interface Sci.*, 2013, **408**, 145–150.
36 S. Shamaila, A. K. L. Sajjad, F. Chen and J. Zhang, *Appl. Catal., B*, 2010, **94**, 272–280.
37 J. Xu, Y. Ao, D. Fu and C. Yuan, *Appl. Surf. Sci.*, 2008, **255**, 2365–2369.
38 A. Hameed, T. Montini, V. Gombac and P. Fornasiero, *J. Am. Chem. Soc.*, 2008, **130**, 9658–9659.
39 Q. Wang, D. Jiao, J. Lian, Q. Ma, J. Yu and H. Huang, *J. Alloys Compd.*, 2015, **649**, 474–482.
40 M. A. Butler and D. S. Ginley, *J. Electrochem. Soc.*, 1978, **125**, 228–232.
41 Agency for Toxic Substances and Disease Registry (ATSDR), *Toxicological Profile for Cresols*, Public Health Service, U.S. Department of Health and Human Services, Atlanta, GA, 1990.
42 R. A. Smith, *Semiconductors*, Cambridge University Press, Cambridge, 2nd edn, 1978.
43 T. Wu, G. Liu, J. Zhoa, H. Hidaka and N. Serpone, *J. Phys. Chem. B*, 1998, **102**, 5845–5851.
44 X. Li and J. Ye, *J. Phys. Chem. C*, 2007, **111**, 13109–13116.
45 O. Merka, V. Yarovyi, D. W. Bahnemann and M. Wark, *J. Phys. Chem. C*, 2011, **115**, 8014–8023.
46 C. Karunakaran and P. Anilkumar, *J. Mol. Catal. A: Chem.*, 2007, **265**, 153–158.
47 S. H. Yoon and J. H. Lee, *Environ. Sci. Technol.*, 2005, **39**, 9695–9701.
48 H. Zhang, R. Zong, J. Zhao and Y. Zhu, *Environ. Sci. Technol.*, 2008, **42**, 3803–3807.

